

R-Meshfusion: Reinforcement Learning Powered Sparse-View Mesh Reconstruction with Diffusion Priors

Haoyang Wang
Peking University
Beijing, China
haoyang.wang@stu.pku.edu.cn

Liming Liu
Peking University
Beijing, China
llm@stu.pku.edu.cn

Peiheng Wang
Peking University
Beijing, China
peiheng.wang@pku.edu.cn

Junlin Hao
Peking University
Beijing, China
junlin.hao@stu.pku.edu.cn

Jiangkai Wu
Peking University
Beijing, China
jiangkai.wu@stu.pku.edu.cn

Xinggong Zhang
Peking University
Beijing, China
zhangxg@pku.edu.cn



Figure 1: Our overall performance. Our method takes sparse-view images as input and produces high-fidelity mesh geometry along with high-quality novel view renderings, showing strong performance in both geometry and appearance.

Abstract

Mesh reconstruction from multi-view images is a fundamental problem in computer vision, but its performance degrades significantly under sparse-view conditions, especially in unseen regions where no ground-truth observations are available. While recent advances in diffusion models have demonstrated strong capabilities in synthesizing novel views from limited inputs, their outputs often suffer from visual artifacts and lack 3D consistency, posing challenges for reliable mesh optimization. In this paper, we propose a novel framework that leverages diffusion models to enhance sparse-view mesh reconstruction in a principled and reliable manner. To address

the instability of diffusion outputs, we propose a Consensus Diffusion Module that filters unreliable generations via interquartile range (IQR) analysis and performs variance-aware image fusion to produce robust pseudo-supervision. Building on this, we design an online reinforcement learning strategy based on the Upper Confidence Bound (UCB) to adaptively select the most informative viewpoints for enhancement, guided by diffusion loss. Finally, the fused images are used to jointly supervise a NeRF-based model alongside sparse-view ground truth, ensuring consistency across both geometry and appearance. Extensive experiments demonstrate that our method achieves significant improvements in both geometric quality and rendering quality.

Permission to make digital or hard copies of all or part of this work for personal or classroom use is granted without fee provided that copies are not made or distributed for profit or commercial advantage and that copies bear this notice and the full citation on the first page. Copyrights for components of this work owned by others than the author(s) must be honored. Abstracting with credit is permitted. To copy otherwise, or republish, to post on servers or to redistribute to lists, requires prior specific permission and/or a fee. Request permissions from permissions@acm.org.

Conference acronym 'XX, Woodstock, NY

© 2025 Copyright held by the owner/author(s). Publication rights licensed to ACM.
ACM ISBN 978-1-4503-XXXX-X/XXXX/XX
<https://doi.org/XXXXXXXX.XXXXXXX>

CCS Concepts

• Computing methodologies → Computer graphics.

Keywords

Sparse-View Mesh Reconstruction, Upper Confidence Bound, Viewpoint Selection, Diffusion Model, Image Fusion

ACM Reference Format:

Haoyang Wang, Liming Liu, Peiheng Wang, Junlin Hao, Jiangkai Wu, and Xinggong Zhang. 2025. R-Meshfusion: Reinforcement Learning Powered Sparse-View Mesh Reconstruction with Diffusion Priors. In *Proceedings of Make sure to enter the correct conference title from your rights confirmation email (Conference acronym 'XX)*. ACM, New York, NY, USA, 9 pages. <https://doi.org/XXXXXXX.XXXXXXX>

1 Introduction

Mesh reconstruction plays a vital role in numerous computer vision and graphics applications, including virtual reality [19], autonomous navigation [10] and cultural heritage preservation [6]. The goal of mesh reconstruction is to recover accurate 3D geometry from multi-view images. However, real-world scenarios often impose limitations, such as constrained capture conditions or limited viewpoints, resulting in sparse-view inputs. This scarcity of views poses significant challenges for mesh reconstruction, often leading to incomplete geometry, blurred surfaces, or missing details, particularly in occluded or unseen regions.

To address these challenges, researchers have explored a spectrum of approaches, evolving from traditional geometry-based pipelines to more recent transformer-based and diffusion-based methods. Traditional methods aim to fully exploit the available ground truth information to enhance multi-view consistency. For example, SfM or MVS-based methods [4, 7] generate point clouds from input views and use them to guide mesh reconstruction. While effective in well-observed regions, these methods struggle to recover details in unseen areas, where no ground truth observations exist.

Transformer-based approaches [11, 29] offer a more global understanding of the input by modeling long-range dependencies across views or sequences. However, these models typically require rich ground truth supervision such as depth maps, normal maps, 3D geometry which are not always available in many practical datasets. As a result, their success heavily relies on generalization from richly supervised training data, making them less effective under sparse-view constraints.

With the recent advances in generative models like Stable Diffusion [24], diffusion-based methods [30, 31, 35] have recently emerged as promising tools for enhancing reconstruction by generating novel views from unseen perspectives. However, existing approaches often struggle to extract sufficiently useful content from these models, limiting their impact on downstream tasks like mesh reconstruction. In many cases, the generated images lack structural coherence, limiting their effectiveness in improving 3D outputs.

Nonetheless, these limitations do not diminish the potential of diffusion models. Recent works [27, 32] demonstrate that when properly conditioned, diffusion models can generate plausible novel views from unseen perspectives. This demonstrates that diffusion models contain rich priors that can be leveraged to enhance mesh reconstruction under sparse-view conditions.

In this paper, we propose a new framework, *R-Meshfusion*, which leverages diffusion models to enhance sparse-view mesh reconstruction by supplementing the sparse ground truth with additional diffusion-generated views. Our key insight is to activate the prior

knowledge embedded in diffusion models to enrich sparse ground-truth data, ultimately improving both geometric and visual fidelity.

However, directly incorporating diffusion-generated views into a reconstruction pipeline introduces several critical challenges. Due to the stochastic nature of diffusion models, the sampling randomness of diffusion models often leads to visual artifacts or unrealistic contents in individual generations. To address this, we introduce a Consensus Diffusion Module that enhances reliability by aggregating multiple diffusion outputs from the same viewpoint. This module filters out inconsistent generations using interquartile range (IQR) analysis and performs variance-aware image fusion to reinforce consistent structures while suppressing unreliable content. The resulting diffusion-guided images serve as robust pseudo-ground-truth supervision for mesh optimization.

While diffusion can enrich sparse-view data, the space of potential viewpoints is continuous and unbounded, and not all views contribute equally to improving reconstruction. Naively sampling viewpoints may result in redundancy or uninformative perspectives. To tackle this challenge, we propose an online viewpoint selection strategy based on the Upper Confidence Bound (UCB), which efficiently explores the view space and adaptively selects informative viewpoints to guide training.

Another challenge arises from the 2D nature of diffusion models. Although they operate in image space, mesh reconstruction demands consistency across multiple views in 3D space. To bridge this gap, we integrate the synthesized views into a NeRF-based training pipeline to jointly optimize geometry and appearance while enforcing multi-view consistency.

We conduct extensive experiments to validate the effectiveness of our approach. The results demonstrate consistent improvements in both geometric quality and rendering quality compared to existing methods.

In summary, the key contributions of our work are as follows:

- We introduce a Consensus Diffusion Module that improves the reliability of diffusion-generated images by filtering out outliers and fusing consistent content via a variance-aware image fusion strategy.
- We propose an online reinforcement learning strategy based on the Upper Confidence Bound (UCB) to adaptively select informative viewpoints to guide training.
- We ensure 3D consistency by incorporating synthesized views into a joint NeRF-based reconstruction framework, improving both geometry and appearance under sparse-view conditions.

2 Related Work

2.1 Sparse View 3D Reconstruction

Sparse view 3D reconstruction has seen significant advancements with the emergence of implicit neural representations, particularly Neural Radiance Fields (NeRF) and Signed Distance Functions (SDF). However, methods based on standard NeRF and SDF [2, 14, 16, 17, 21, 28, 33] require dense views for effective supervision and struggles under sparse view settings due to overfitting and lack of sufficient constraints. Various adaptations [5, 7, 12, 20] have been proposed to address these limitations, incorporating additional priors such as depth supervision, multi-view consistency,

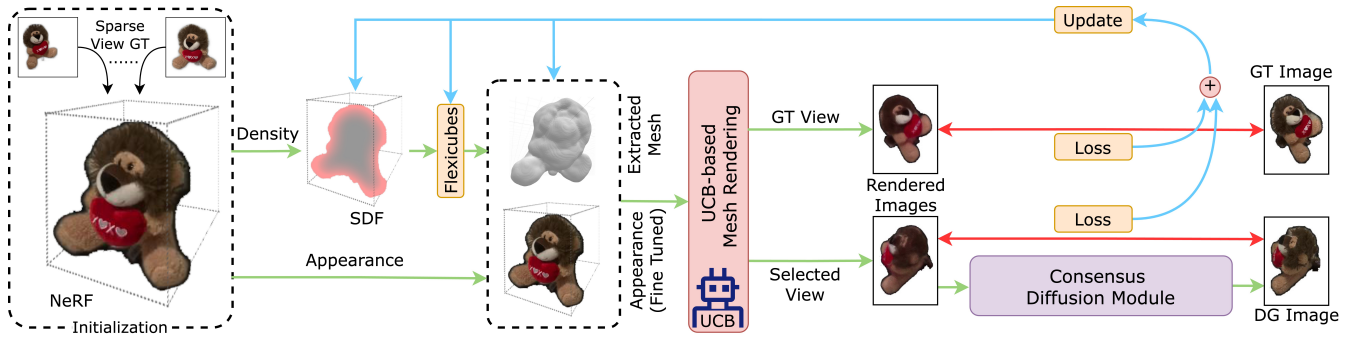


Figure 2: Our framework, *R-Meshfusion*. We adopt a two-stage, coarse-to-fine training process for mesh reconstruction. In stage 1, we initialize the geometry and view-dependent appearance representation based on NeRF. This initial phase results in a coarse SDF grid and an initial view-dependent appearance model. Then in stage 2, we leverage a pretrained conditioned diffusion model and apply knowledge distillation for further mesh refinement. For each training iteration, we take three steps. We first select the optimal viewpoint based on UCB strategy to render the corresponding image from mesh. We then apply our proposed Consensus Diffusion Module to obtain a higher-quality diffusion-guided (DG) image. Finally, we simultaneously refine both the geometry and the appearance representation. After training is complete, we obtain the final mesh.

and uncertainty modeling to improve reconstruction fidelity under sparse inputs. In our method, we leverage NeRF for initialization and SDF for mesh refinement, with both components playing a key role in enforcing 3D consistency across views. Beyond implicit representations, more recent advances in diffusion model [30, 31, 35] have been explored to learn powerful shape priors from data, enabling the synthesis of plausible geometry from very few input views. However, their outputs often suffer from artifacts by directly using diffusion outputs for supervision or geometry prediction. Our approach leverages a diffusion prior to guide mesh refinement through a consensus-driven and viewpoint-adaptive framework, improving reconstruction quality under limited supervision. Meanwhile, transformer-based [11, 29] approaches have demonstrated strong capabilities in multi-view feature aggregation, utilizing self-attention and cross-view feature fusion to enhance consistency across sparse observations. However, these methods often require dense feature supervision or strong view correspondences, which limits their effectiveness under extremely sparse-view settings. In contrast, our approach leverages learned diffusion priors to inject high-level knowledge, reducing the need for extensive supervision and enabling more robust reconstruction from limited views.

2.2 Best Views Selection in 3D Scenes

Selecting best views in 3D scenes is a critical issue in computer vision and 3D reconstruction, directly impacting the quality of final rendering and model reconstructions. Traditional approaches often rely on heuristic or predetermined viewpoint strategies, which may not adapt well to dynamically changing environments or complex scene structures. Some recent works [8, 9, 22] in radiance fields incorporate uncertainty estimation to guide the selection process. However, these approaches are based on ray sampling in radiance fields training, which are less applicable to our focus on surface mesh reconstruction. Additionally, several studies concentrate on the field of next best view (NBV) planning [10, 13, 18], which is

primarily applied in the robotic exploration of unknown environments. These works aim to optimize the reconstruction of the new scene by selecting the minimal number of viewpoints necessary for comprehensive coverage. However, our objective is to enhance the observational perspective by online selecting the optimal viewpoints based on existing training viewpoints and their performance gains.

3 Preliminaries

3.1 Neural Radiance Field (NeRF)

Neural Radiance Field (NeRF) is a framework for representing 3D scenes using neural networks. Given a 3D point $\mathbf{x} \in \mathbb{R}^3$ and a viewing direction $\mathbf{d} \in \mathbb{R}^3$, NeRF learns a function $F_\theta(\mathbf{x}, \mathbf{d})$ parameterized by a neural network that predicts the volume density σ and view-dependent color \mathbf{c} :

$$F_\theta(\mathbf{x}, \mathbf{d}) = (\sigma, \mathbf{c}). \quad (1)$$

To render an image, NeRF employs volume rendering, where the color of a pixel is computed by integrating the color and density along a camera ray $\mathbf{r}(t) = \mathbf{o} + t\mathbf{d}$, where \mathbf{o} is the camera origin. The pixel color is approximated using the following discrete formulation:

$$C(\mathbf{r}) = \sum_{i=1}^N T_i (1 - e^{-\sigma_i \delta_i}) \mathbf{c}_i, \quad (2)$$

where T_i is the accumulated transmittance:

$$T_i = \exp\left(-\sum_{j=1}^{i-1} \sigma_j \delta_j\right), \quad (3)$$

and δ_i is the distance between consecutive sample points along the ray.

To optimize the model, NeRF is trained using a set of posed images and learns to render novel views by minimizing the reconstruction error between rendered and ground-truth images. Given

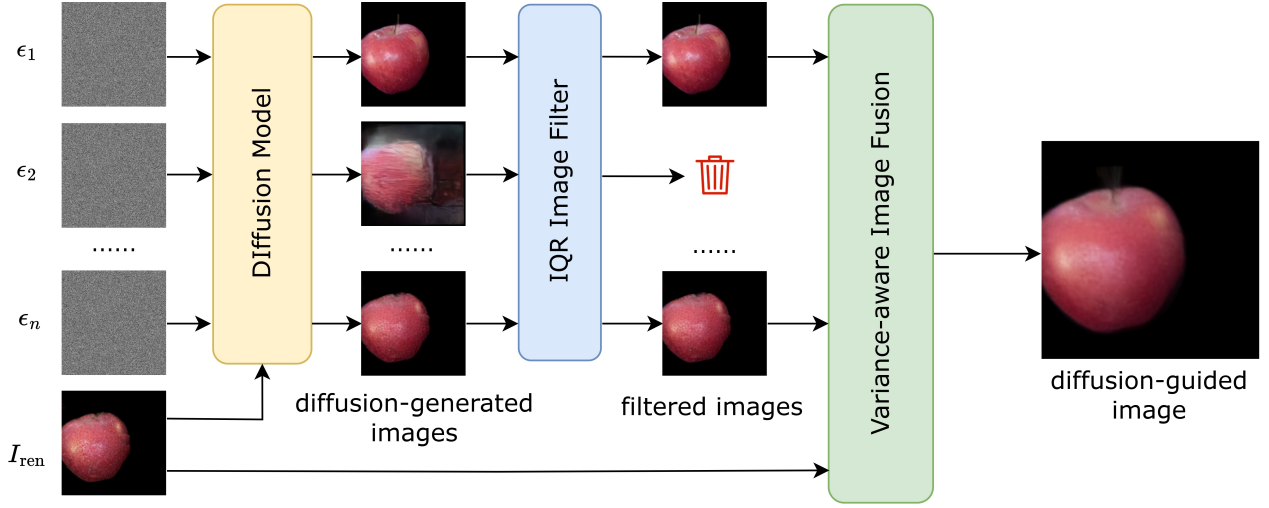


Figure 3: Illustration of our Consensus Diffusion Module.

a set of ground-truth pixel colors C_i^{GT} corresponding to sampled rays \mathbf{r}_i , the training loss is defined as:

$$L = \sum_i \|C(\mathbf{r}_i) - C_i^{\text{GT}}\|_2^2. \quad (4)$$

where $C(\mathbf{r}_i)$ is the rendered pixel color obtained via volume rendering.

3.2 Denoising Diffusion Models (DDMs)

Denoising diffusion models (DDMs) are a class of generative models that have achieved tremendous performance in various image generation tasks. In our work, we utilize DDMs for image enhancement, where an input image is combined with noise, and the model generates a denoised output. Here, we introduce the generation process of DDMs, which includes forward process and reverse process.

3.2.1 Forward Process. The forward process gradually adds Gaussian noise $\epsilon \sim \mathcal{N}(0, I)$ to a data sample $x_0 \sim q(x_0)$ over T time steps, producing a sequence x_1, \dots, x_T . The process is defined as follows:

$$q(x_t|x_{t-1}) = \mathcal{N}(x_t; \sqrt{1 - \beta_t}x_{t-1}, \beta_t I), \quad (5)$$

where β_t is a predefined noise schedule.

By recursively applying the reparameterization, we can express x_t directly in terms of x_0 :

$$q(x_t|x_0) = \mathcal{N}(x_t; \sqrt{\bar{\alpha}_t}x_0, (1 - \bar{\alpha}_t)I), \quad (6)$$

where $\alpha_t = 1 - \beta_t$ and $\bar{\alpha}_t = \prod_{s=1}^t \alpha_s$.

Equivalently, x_t can be rewritten as:

$$x_t = \sqrt{\bar{\alpha}_t}x_0 + \sqrt{1 - \bar{\alpha}_t}\epsilon, \quad (7)$$

3.2.2 Reverse Process. The reverse process learns to denoise x_t back to x_0 by parameterizing a learned model $p_\theta(x_{t-1}|x_t)$:

$$p_\theta(x_{t-1}|x_t) = \mathcal{N}(x_{t-1}; \mu_\theta(x_t, t), \Sigma_\theta(x_t, t)). \quad (8)$$

The mean μ_θ is commonly predicted via a neural network trained to minimize the variational lower bound or the noise prediction objective.

The sampling process progressively denoises using:

$$x_{t-1} = \mu_\theta(x_t, t) + \sigma_t \epsilon, \quad \epsilon \sim \mathcal{N}(0, I), \quad (9)$$

iterating until x_0 is obtained as the final generated sample.

3.2.3 Conditioned Diffusion Model. In our work, we utilize a conditioned diffusion model where the forward process and reverse process incorporate additional conditioning information c . The modified forward process is given by:

$$q(x_t|x_{t-1}, c) = \mathcal{N}(x_t; \sqrt{1 - \beta_t}x_{t-1}, \beta_t I). \quad (10)$$

Similarly, the direct formulation in terms of x_0 with conditioning is:

$$q(x_t|x_0, c) = \mathcal{N}(x_t; \sqrt{\bar{\alpha}_t}x_0, (1 - \bar{\alpha}_t)I). \quad (11)$$

The corresponding reparameterized form remains:

$$x_t = \sqrt{\bar{\alpha}_t}x_0 + \sqrt{1 - \bar{\alpha}_t}\epsilon. \quad (12)$$

The conditional reverse process modifies the denoising step to condition on c :

$$p_\theta(x_{t-1}|x_t, c) = \mathcal{N}(x_{t-1}; \mu_\theta(x_t, t, c), \Sigma_\theta(x_t, t, c)). \quad (13)$$

In the conditional case, the sampling follows:

$$x_{t-1} = \mu_\theta(x_t, t, c) + \sigma_t \epsilon, \quad \epsilon \sim \mathcal{N}(0, I), \quad (14)$$

iterating from T to 0 to obtain the final generated sample x_0 that respects the given condition c .

4 Method

4.1 Framework

In this section, we introduce our framework, *R-Meshfusion*, as illustrated in Fig. 2. We adopt a two-stage, coarse-to-fine training process for mesh reconstruction. In stage 1, we use Instant-NGP [16] as the underlying NeRF architecture. Given a set of sparse input images, Instant-NGP initializes both the geometry and the color representation of the mesh, producing a coarse SDF grid and an initial view-dependent appearance model. In stage 2, we leverage the pretrained conditioned diffusion model from [35] and apply

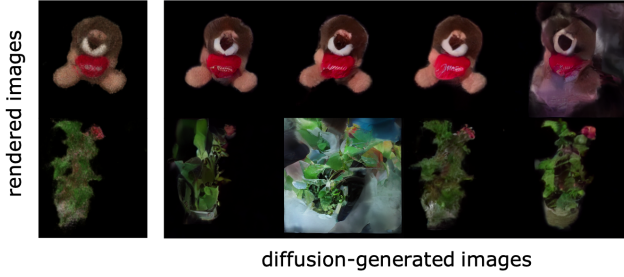


Figure 4: Illustration of a mesh-rendered image on the left, followed by diffusion-generated images on the right.

knowledge distillation for further mesh refinement (Section 4.2). For each training iteration, we take three key steps. First, we select the optimal rendering viewpoint based on UCB values and render the corresponding images from the mesh, which are then fed into a diffusion model for enhancement (Section 4.4). We then apply our Consensus Diffusion Module, depicted in Fig. 3, to filter unreliable generations and fuse consistent outputs to enhance the reliability of the diffusion-generated images, resulting in high-quality diffusion-guided images (Section 4.3). Based on these images, we simultaneously optimize both the geometry and the appearance representation. Upon completion of the training, we utilize xatlas [34] for UV unwrapping and export the resulting object mesh.

4.2 Knowledge Distillation for Enhanced 3D Reconstruction

Due to the sparse-view observations, the rendering quality for unseen viewpoints is significantly degraded. Therefore, in addition to the sparse-view ground truth supervision, we also leverage the knowledge distilled from the diffusion model to guide the refinement.

Given a target novel view π and a set of sparse-view input images C , we utilize epipolar feature transformer (EFT) from [35] to extract a feature grid $y = h(\pi, C)$. For the mesh-rendered image at view π , denoted as $x = f(\pi)$, we encode it into the latent space as $z = \text{Enc}(x)$. We then employ the pretrained view-conditioned latent diffusion model (VLDM) to predict the posterior $p_\theta(z|\pi, C)$, generating a refined latent representation \hat{z} , which is decoded to obtain the diffusion-generated image $\hat{x} = \text{Dec}(\hat{z})$.

To enforce consistency between the rendered image x and the diffusion-generated image \hat{x} , we define a diffusion loss that combines MSE and LPIPS loss:

$$L_{\text{diff}} = \lambda_{\text{MSE}} \|x - \hat{x}\|_2^2 + \lambda_{\text{LPIPS}} \text{LPIPS}(x, \hat{x}). \quad (15)$$

We use this loss function to help optimize both the SDF and appearance representations, ensuring improved reconstruction quality and perceptual consistency, especially in unseen viewpoints.

4.3 Consensus Diffusion Module

Due to sparse-view inputs, we adopt a pretrained diffusion model to enhance mesh-rendered images, with the goal of restoring fine details and improving supervision for mesh optimization. However,

a critical challenge arises from the stochastic nature of diffusion models: individual outputs may be noisy or unreliable, especially for unseen viewpoints, as shown in Fig. 4. Relying on a single diffusion sample can thus lead to unstable model optimization.

To address this, we propose the Consensus Diffusion Module. Our key insight is to extract stable, high-fidelity supervision by forming consensus and seeking agreement across multiple diffusion samples. Rather than treating all generated images equally, we selectively filter and adaptively fuse them to emphasize reliable regions and suppress outliers. This framework consists of two core components: an IQR-based image filter for removing inconsistent diffusion outputs, and a variance-aware image fusion strategy that adaptively blends results based on pixel-wise agreement.

4.3.1 IQR Image Filter. The first step in forming consensus is identifying and removing outlier diffusion outputs that may corrupt the fusion process. Given a mesh-rendered image I_{ren} , we generate a set of diffusion-generated images $\{I_{\text{diff}}^{(i)}\}_{i=1}^N$ by the diffusion model by feeding the diffusion model with N different noise inputs $\{\epsilon_i\}_{i=1}^N$ sampled from $\mathcal{N}(0, 1)$. We compute the loss (defined in Eq. 15) for each diffusion-generated image compared to the original rendered image, removing images whose losses fall outside the acceptable range defined as:

$$[0, Q_3 + 1.5 \times \text{IQR}], \quad (16)$$

where Q_i denote the i -th quartiles of the reconstruction losses and $\text{IQR} = Q_3 - Q_1$.

After filtering, we obtain a refined set of diffusion-generated images $\{I_{\text{diff}}^{(j)}\}_{j=1}^M$ that better represents the consensual visual structure shared across the stochastic samples, where $M \leq N$. Through this, we prevent a small number of poor-quality generations from distorting the estimated reliability of each pixel.

4.3.2 Variance-aware Image Fusion. After filtering, we aim to aggregate the retained diffusion samples into a single image that reflects the shared consensus while accounting for spatial uncertainty. For each pixel location, the variance of the corresponding intensity values across the filtered diffusion-generated images indicate the level of disagreement among the samples. To quantify the degree of agreement, we compute a pixel-wise variance map over the filtered set:

$$\sigma^2(x, y) = \frac{1}{M} \sum_{i=1}^M \left(I_{\text{diff}}^{(i)}(x, y) - \bar{I}_{\text{diff}}(x, y) \right)^2, \quad (17)$$

where $\bar{I}_{\text{diff}}(x, y)$ is the pixel-wise mean image computed as:

$$\bar{I}_{\text{diff}}(x, y) = \frac{1}{M} \sum_{i=1}^M I_{\text{diff}}^{(i)}(x, y). \quad (18)$$

Intuitively, pixels with high variance reflect disagreement among samples and thus lower confidence, while pixels with low variance show a strong consensus.

Then, we transform the variance map into a normalized confidence map $V(x, y)$ using a sigmoid function:

$$V(x, y) = 1 - \frac{1}{1 + e^{-(\alpha(\sigma^2(x, y) - \beta))}}, \quad (19)$$

Finally, we perform confidence-guided fusion between the mesh-rendered image and the averaged diffusion-generated image based

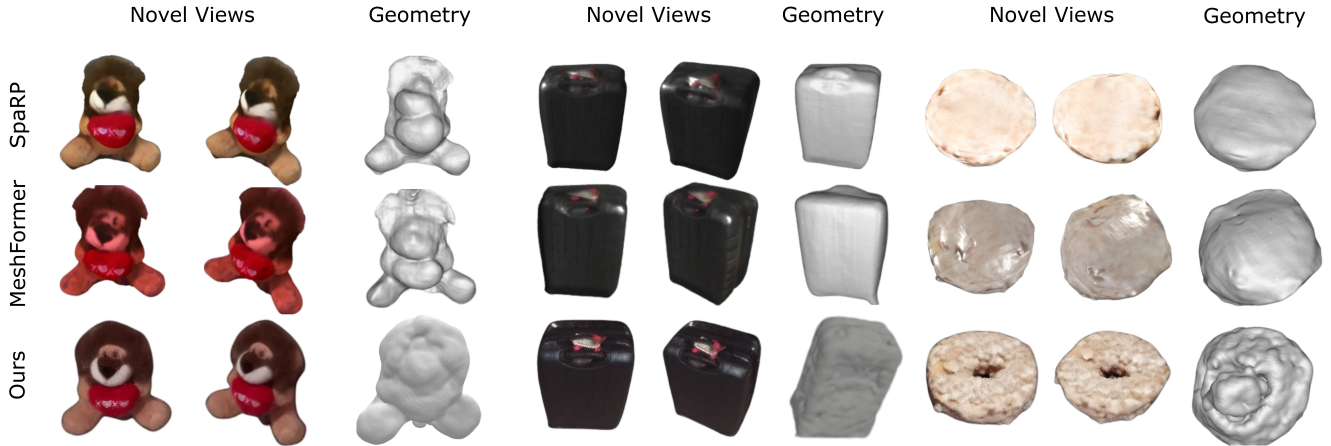


Figure 5: Qualitative comparison of mesh rendering quality and geometry among our method and baselines. Under sparse-view inputs, our method achieves superior visual fidelity and more accurate geometry.

on the confidence map to obtain the final fused image I_{fusion} :

$$I_{\text{fusion}}(x, y) = V(x, y) \cdot I_{\text{ren}}(x, y) + (1 - V(x, y)) \cdot \tilde{I}_{\text{diff}}(x, y). \quad (20)$$

This pixel-adaptive fusion based on local consensus can mitigate stochastic artifacts introduced by the diffusion model, thereby obtaining higher-quality diffusion-guided images for optimizing the 3D mesh model.

4.4 UCB-based Mesh Rendering

To further enhance the quality and efficiency of mesh reconstruction under sparse-view settings, we propose a UCB-Based Mesh Rendering strategy. This module aims to guide mesh optimization with both static sparse-view supervision and actively selected viewpoints using a UCB strategy. The key idea is to dynamically identify and render informative viewpoints that are most beneficial for supervision. Moreover, when such views lack ground truth images, we leverage the Consensus Diffusion Module to produce reliable pseudo-supervision, enabling consistent optimization signals across both observed and unobserved views.

4.4.1 UCB-based Adaptive Viewpoint Selection. Given a sparse set of input views, the quality of the reconstructed 3D scene heavily depends on the diversity and informativeness of the selected viewpoints. To achieve high-fidelity reconstruction, it is crucial to strategically select the novel view to be enhanced by the diffusion model, providing the most valuable information. The core challenge lies in efficiently selecting the novel view that maximize the information gain while minimizing redundancy.

During the training process, the model parameters and the rendering losses of each training viewpoint are continuously varying, it is not optimal to select a fixed viewpoint to be enhanced by the diffusion model throughout the training process. To address this issue, we propose an online reinforcement learning strategy to adaptively select the optimal viewpoint in each training iteration considering the current state of the model and the performance gains from previously selected viewpoints.

Many state-of-the-art reinforcement RL methods, such as DQN [15] and PPO [25], introduce additional networks for inference, which results in significant time overhead. In contrast, our strategy using UCB does not require neural networks for inference, thereby reducing computational complexity and speeding up the decision-making process.

Given sparse input viewpoints v_1, v_2, \dots, v_m , we first interpolate n intermediate viewpoints to enrich the set of candidate views. These interpolated viewpoints, along with the original sparse viewpoints, constitute the action space $\mathcal{A} = \{a_1, a_2, \dots, a_{m+n}\}$, where each action a_i corresponds to selecting a specific viewpoint for rendering and subsequent enhancement. The UCB value for each action is calculated as follows:

$$\text{UCB}_a(t) = \hat{r}_a(t) + c \sqrt{\frac{2 \ln t}{N_a(t)}}, \quad (21)$$

where $\hat{r}_a(t)$ represents the empirical mean reward for action a up to time t , c is a constant controlling the degree of exploration, t represents the total number of steps t , and $N_a(t)$ denotes the number of times action a has been selected. Here, time t specifically refers to the t -th iteration in the stage 2 training process. At initialization, the UCB value for each action is set to a large value, ensuring that every action is explored at least once.

For each training iteration, we select the optimal action that maximizes the UCB value:

$$a_t = \arg \max_a \text{UCB}_a(t), \quad (22)$$

During the t -th iteration, we select the optimal action and render the corresponding viewpoint image, which is then enhanced using the diffusion model. The fusion loss is computed to optimize the model.

To design an effective reward function for the action, we aim to quantify the value of that viewpoint under the current mesh state.

For each selected viewpoint a , we render the current mesh to obtain $I_{\text{ren}}^{(a)}$, and generate a pseudo-ground-truth image $I_{\text{fusion}}^{(a)}$ via

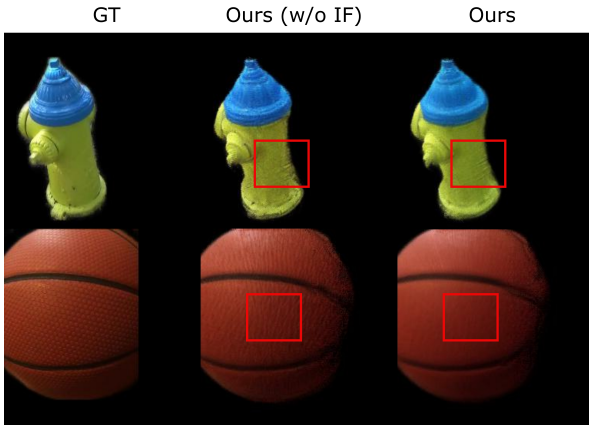


Figure 6: Rendering quality with (right) and without (middle) image fusion (IF). IF critically preserves fine details and reduces blurred artifacts.

the *Consensus Diffusion Module*. The diffusion loss is computed by Eq. 15:

$$L_{\text{diff}}(a) = \lambda_{\text{MSE}} \|I_{\text{ren}}^{(a)} - I_{\text{fusion}}^{(a)}\|_2^2 + \lambda_{\text{LPIPS}} \text{LPIPS}(I_{\text{ren}}^{(a)}, I_{\text{fusion}}^{(a)}). \quad (23)$$

We define the reward as the diffusion loss itself:

$$r(a) = L_{\text{diff}}(a). \quad (24)$$

By prioritizing high-loss views, the UCB-based selection policy actively seeks out informative errors, allowing the mesh to improve more efficiently through targeted supervision.

4.5 Joint Optimization For 3D Consistency

In the first stage, we use Instant-NGP architecture to efficiently train a NeRF model for initializing 3D scene information. The geometry and appearance representation are learned through a multi-resolutional density grid combined with a shallow Multilayer Perceptron (MLP).

After completing the training, we extract a density grid at a predefined resolution and transform it into an SDF grid. The density value, which quantifies the material concentration at a given point, is inherently non-negative. In contrast, the SDF encodes the shortest distance to the nearest surface, taking both positive and negative values to differentiate between interior and exterior regions. To achieve this conversion, we define an iso-surface threshold θ and compute the corresponding coarse SDF grid using the following formula:

$$\text{SDF} = \begin{cases} \frac{\sigma - \theta}{\max(\sigma) - \theta}, & \text{if } \sigma > \theta \\ \frac{\sigma - \theta}{\theta}, & \text{otherwise} \end{cases} \quad (25)$$

where σ represents the density value at a point, and θ represents the iso-surface.

This process generates the initial SDF grid, which is subsequently refined in stage 2.

In the second stage, we perform refinement of the SDF grid and the appearance representation based on the surface rendering of the mesh. We adopt FlexiCubes [26] to differentially extract the

Table 1: Rendering quality comparisons on the CO3Dv2 dataset. Compared to baselines, our method achieves better rendering quality.

Method	PSNR \uparrow	SSIM \uparrow	LPIPS \downarrow
MeshFormer [11]	22.75	0.73	0.256
SpaRP [31]	22.13	0.72	0.264
Ours	23.72	0.78	0.244

Table 2: Ablation study of our design choices. The results show that both the image fusion (IF) and viewpoint selection (VS) improve the overall performances.

IF	VS	PSNR \uparrow	SSIM \uparrow	LPIPS \downarrow
\checkmark	\checkmark	23.72	0.78	0.244
\checkmark	\times	23.60	0.78	0.246
\times	\checkmark	23.39	0.77	0.246
\times	\times	23.30	0.77	0.249

mesh from the SDF and nvdiffrast [17] to perform differentiable rendering, ensuring the continuity of gradient flow.

The core of FlexiCubes involves adding two attributes to each vertex in an SDF grid, namely weight and deformation, ensuring the SDF grid is deformable. These attributes allow for the extraction of a mesh’s geometry based on positions of grid vertices and their respective SDF values. After extracting the mesh from the SDF grid, its appearance is determined by querying the appearance field. The mesh is then rendered using nvdiffrast and we optimize both the geometry and appearance representation by leveraging multiple loss functions. We apply supervision from both the ground truth and the diffusion-guided images, ensuring high-fidelity reconstruction with improved 3D consistency.

To optimize the parameters, we use the following overall loss function:

$$L = \lambda_{\text{color}} L_{\text{color}}(x) + \lambda_{\text{TV}} L_{\text{TV}} + \lambda_{\text{dev}} L_{\text{dev}} + \lambda_{\text{diff}} L_{\text{diff}}, \quad (26)$$

where $L_{\text{color}}(x) = \sqrt{(x - x^*)^2 + \epsilon^2}$ is the Charbonnier loss [1], measuring the discrepancy between the predicted and ground-truth images, with ϵ improving robustness to outliers. L_{TV} is the Total Variation (TV) regularization term [3], which helps suppress floaters and promote smoothness in the SDF grid. L_{dev} is the FlexiCubes regularizer to mitigate mesh artifacts. L_{diff} is the diffusion loss, as defined in Eq. 15.

5 Experiments

5.1 Implementation Details

5.1.1 Datasets. To evaluate our approach and baseline approaches, we use 10 scenes from the real-world from the CO3Dv2 dataset [23] to assess both the reconstructed mesh quality and the rendering quality. Experimental results demonstrate that our approach achieves excellent rendering and mesh reconstruction outcomes across most scenes.

Table 3: Ablation study of our image fusion strategy.

Fusion Strategy	PSNR \uparrow	SSIM \uparrow	LPIPS \downarrow
Ours	23.72	0.78	0.244
max pixel loss	23.29	0.75	0.261
min pixel loss	23.55	0.76	0.252
min image loss	23.71	0.78	0.246
max image loss	23.38	0.75	0.259
Ours (w/o IQR)	23.64	0.77	0.245

Table 4: Ablation study of our viewpoint selection strategy.

Strategy	PSNR \uparrow	SSIM \uparrow	LPIPS \downarrow
Ours	23.72	0.78	0.244
Random	23.60	0.78	0.246
Sequential	23.48	0.76	0.248

5.1.2 Training Details. In the first stage, we train the NeRF model for 30,000 steps. At the end of the training, we extract an SDF grid at a resolution of 128^3 . For stage 2, we train the model for 3,000 steps to ensure that both the UCB and the model converge. The optimizer used is Adam, with the learning rates for both the Flexi-Cubes parameters and the SDF set to 1×10^{-4} . The experiments are all conducted on a high-performance computing platform equipped with a GeForce RTX 3090 GPU.

5.1.3 Baselines. We compare our method against recent baselines for sparse-view reconstruction: MeshFormer [11] and SpaRP [31]. MeshFormer is a transformer-based approach for multi-view mesh prediction. SpaRP produces a 3D textured mesh from sparse views through a diffusion model. All baselines are evaluated under the same sparse-view setting as our method, where the input consists of 6 randomly selected viewpoints.

5.2 Evaluation

5.2.1 Geometric Quality. To evaluate the geometric accuracy of our mesh reconstructions, we establish MeshFormer, SpaRP as baselines for our experiments and find that our results significantly outperform the previous works. Fig. 5 presents qualitative comparisons of our mesh reconstruction, demonstrating enhanced rendering realism and geometric accuracy, along with richer and more detailed surface structures.

5.2.2 Rendering Quality. We employ PSNR, SSIM (Structural Similarity Index Measure), and LPIPS (Learned Perceptual Image Patch Similarity) metrics to evaluate the rendering quality of our mesh reconstruction. Compared to baselines, our methodology demonstrated superior performance in the majority of the tested scenes. The detailed results of this comparative analysis are presented in Table 1 and Fig. 5. These metrics highlight our approach’s advancements in delivering high-fidelity reconstructions across various complex scenarios.

5.3 Ablation Studies

To evaluate the contributions of each component in our framework, we perform an ablation study focusing on the image fusion strategy and the viewpoint selection mechanism. Specifically, we compare the performance of full model against variants excluding image fusion (IF) and viewpoint selection (VS), and further assess the impact of different design choices within each component.

As shown in Table 2, when viewpoint selection is removed, the rendering quality noticeably decreases, primarily because the model loses the ability to incorporate diverse and informative perspectives that contribute to more detailed and accurate reconstructions. When image fusion is further removed, the quality declines even more significantly (Fig. 6), as the supervision relies on a single generated image, which increases the likelihood of unrealistic content due to the stochastic nature of diffusion models.

For the image fusion strategy, we experiment with four variants based on the reconstruction loss between the diffusion-generated images and the mesh-rendered image: max pixel loss, min pixel loss, max image loss, and min image loss. The max and min pixel loss strategies select the supervision signal from the image with the highest or lowest per-pixel reconstruction error, respectively. In contrast, the max and min image loss strategies choose the entire image with the highest or lowest total reconstruction loss to supervise the mesh refinement. Additionally, we include a variant of our method without the IQR image filtering step, to assess the impact of outlier rejection on the fusion quality. As shown in Table 3, our full fusion strategy outperforms the alternative variants.

For viewpoint selection, our method incrementally selects one informative view at each iteration, based on the current state of the reconstruction. This adaptive, round-by-round selection allows the model to focus supervision on views that are most beneficial at each stage of training. To assess its effectiveness, we compare it with two alternatives: random selection and sequential selection. The random and sequential strategies do not consider informativeness or spatial coverage, while the version without distance reward selects views solely based on image-level supervision. Table 4 shows that our UCB-based strategy achieves better results by selecting views that are both informative and spatially diverse.

6 Limitation and Conclusion

Although our proposed method shows improvements in rendering quality and mesh reconstruction compared to previous work, there are several limitations to consider. We use shallow MLPs and an appearance feature grid to model view-dependent effects. However, this approach may struggle to effectively capture complex view-dependent components and fails to represent semi-transparent effects in scenes.

In this work, we present *R-Meshfusion*, a novel framework for sparse-view mesh reconstruction that leverages diffusion models to synthesize informative novel views. To effectively utilize diffusion priors under sparse supervision, we propose a Consensus Diffusion Module that enhances the reliability of generated images through outlier filtering and variance-aware fusion, producing high-quality diffusion-guided images. In addition, we introduce an online UCB-based viewpoint selection strategy to actively explore the view

space and identify the most informative perspectives for super-resolution. These components are integrated into a joint NeRF-based reconstruction pipeline, ensuring 3D consistency across geometry and appearance. Extensive experiments demonstrate that our method substantially improves both geometric accuracy and rendering quality under challenging sparse-view conditions.

References

- [1] Jonathan T Barron, Ben Mildenhall, Dor Verbin, Pratul P Srinivasan, and Peter Hedman. 2022. Mip-nerf 360: Unbounded anti-aliased neural radiance fields. In *Proceedings of the IEEE/CVF conference on computer vision and pattern recognition*. 5470–5479.
- [2] Jonathan T Barron, Ben Mildenhall, Dor Verbin, Pratul P Srinivasan, and Peter Hedman. 2023. Zip-nerf: Anti-aliased grid-based neural radiance fields. In *Proceedings of the IEEE/CVF International Conference on Computer Vision*. 19697–19705.
- [3] Anpei Chen, Zexiang Xu, Andreas Geiger, Jingyi Yu, and Hao Su. 2022. Tensorf: Tensorial radiance fields. In *European conference on computer vision*. Springer, 333–350.
- [4] Anpei Chen, Zexiang Xu, Fuqiang Zhao, Xiaoshuai Zhang, Fanbo Xiang, Jingyi Yu, and Hao Su. 2021. Mvnerf: Fast generalizable radiance field reconstruction from multi-view stereo. In *Proceedings of the IEEE/CVF international conference on computer vision*. 14124–14133.
- [5] Kangle Deng, Andrew Liu, Jun-Yan Zhu, and Deva Ramanan. 2022. Depth-supervised nerf: Fewer views and faster training for free. In *Proceedings of the IEEE/CVF conference on computer vision and pattern recognition*. 12882–12891.
- [6] Leonardo Gomes, Olga Regina Pereira Bellon, and Luciano Silva. 2014. 3D reconstruction methods for digital preservation of cultural heritage: A survey. *Pattern Recognition Letters* 50 (2014), 3–14.
- [7] Han Huang, Yulun Wu, Junsheng Zhou, Ge Gao, Ming Gu, and Yu-Shen Liu. 2024. Neusurf: On-surface priors for neural surface reconstruction from sparse input views. In *Proceedings of the AAAI conference on artificial intelligence*, Vol. 38. 2312–2320.
- [8] Liren Jin, Xieyuanli Chen, Julius Rückin, and Marija Popović. 2023. Neu-nbv: Next best view planning using uncertainty estimation in image-based neural rendering. In *2023 IEEE/RSJ International Conference on Intelligent Robots and Systems (IROS)*. IEEE, 11305–11312.
- [9] Hyunseo Kim, Hyeonseo Yang, Taekyung Kim, YoonSung Kim, Jin-Hwa Kim, and Byoung-Tak Zhang. 2024. ActiveNeuS: Active 3D Reconstruction using Neural Implicit Surface Uncertainty. *arXiv preprint arXiv:2405.02568* (2024).
- [10] Michael Krainin, Brian Curless, and Dieter Fox. 2011. Autonomous generation of complete 3D object models using next best view manipulation planning. In *2011 IEEE international conference on robotics and automation*. IEEE, 5031–5037.
- [11] Minghua Liu, Chong Zeng, Xinyue Wei, Ruoxi Shi, Linghao Chen, Chao Xu, Mengqi Zhang, Zhaoning Wang, Xiaoshuai Zhang, Isabella Liu, et al. 2024. Mesh-former: High-quality mesh generation with 3d-guided reconstruction model. *arXiv preprint arXiv:2408.10198* (2024).
- [12] Xiaoxiao Long, Cheng Lin, Peng Wang, Taku Komura, and Wenping Wang. 2022. Sparseneus: Fast generalizable neural surface reconstruction from sparse views. In *European Conference on Computer Vision*. Springer, 210–227.
- [13] Christopher McCreavy, Lars Kunze, and Nick Hawes. 2017. Next best view planning for object recognition in mobile robotics. In *CEUR Workshop Proceedings*, Vol. 1782. CEUR Workshop Proceedings.
- [14] Ben Mildenhall, Pratul P Srinivasan, Matthew Tancik, Jonathan T Barron, Ravi Ramamoorthi, and Ren Ng. 2021. Nerf: Representing scenes as neural radiance fields for view synthesis. *Commun. ACM* 65, 1 (2021), 99–106.
- [15] Volodymyr Mnih, Koray Kavukcuoglu, David Silver, Andrei A Rusu, Joel Veness, Marc G Bellemare, Alex Graves, Martin Riedmiller, Andreas K Fidjeland, Georg Ostrovski, et al. 2015. Human-level control through deep reinforcement learning. *nature* 518, 7540 (2015), 529–533.
- [16] Thomas Müller, Alex Evans, Christoph Schied, and Alexander Keller. 2022. Instant neural graphics primitives with a multiresolution hash encoding. *ACM transactions on graphics (TOG)* 41, 4 (2022), 1–15.
- [17] Jacob Munkberg, Jon Hasselgren, Tianchang Shen, Jun Gao, Wenzheng Chen, Alex Evans, Thomas Müller, and Sanja Fidler. 2022. Extracting triangular 3d models, materials, and lighting from images. In *Proceedings of the IEEE/CVF Conference on Computer Vision and Pattern Recognition*. 8280–8290.
- [18] Menaka Naazare, Francisco Garcia Rosas, and Dirk Schulz. 2022. Online next-best-view planner for 3D-exploration and inspection with a mobile manipulator robot. *IEEE Robotics and Automation Letters* 7, 2 (2022), 3779–3786.
- [19] Francisco Navarro, Javier Fdez, Mario Garzón, Juan Jesús Roldán, and Antonio Barrientos. 2018. Integrating 3D reconstruction and virtual reality: A new approach for immersive teleoperation. In *ROBOT 2017: Third Iberian Robotics Conference: Volume 2*. Springer, 606–616.
- [20] Michael Niemeyer, Jonathan T Barron, Ben Mildenhall, Mehdi SM Sajjadi, Andreas Geiger, and Noha Radwan. 2022. Regnerf: Regularizing neural radiance fields for view synthesis from sparse inputs. In *Proceedings of the IEEE/CVF conference on computer vision and pattern recognition*. 5480–5490.
- [21] Michael Oechsle, Songyou Peng, and Andreas Geiger. 2021. Unisurf: Unifying neural implicit surfaces and radiance fields for multi-view reconstruction. In *Proceedings of the IEEE/CVF International Conference on Computer Vision*. 5589–5599.
- [22] Xuran Pan, Zihang Lai, Shiji Song, and Gao Huang. 2022. Activenerf: Learning where to see with uncertainty estimation. In *European Conference on Computer Vision*. Springer, 230–246.
- [23] Jeremy Reizenstein, Roman Shapovalov, Philipp Henzler, Luca Sbordone, Patrick Labatut, and David Novotny. 2021. Common objects in 3d: Large-scale learning and evaluation of real-life 3d category reconstruction. In *Proceedings of the IEEE/CVF international conference on computer vision*. 10901–10911.
- [24] Robin Rombach, Andreas Blattmann, Dominik Lorenz, Patrick Esser, and Björn Ommer. 2022. High-resolution image synthesis with latent diffusion models. In *Proceedings of the IEEE/CVF conference on computer vision and pattern recognition*. 10684–10695.
- [25] John Schulman, Filip Wolski, Prafulla Dhariwal, Alec Radford, and Oleg Klimov. 2017. Proximal policy optimization algorithms. *arXiv preprint arXiv:1707.06347* (2017).
- [26] Tianchang Shen, Jacob Munkberg, Jon Hasselgren, Kangxue Yin, Zian Wang, Wenzheng Chen, Zan Gojcic, Sanja Fidler, Nicholas Sharp, and Jun Gao. 2023. Flexible Isosurface Extraction for Gradient-Based Mesh Optimization. *ACM Trans. Graph.* 42, 4 (2023), 37–1.
- [27] Vikram Voleti, Chun-Han Yao, Mark Boss, Adam Letts, David Pankratz, Dmitry Tochilkin, Christian Laforte, Robin Rombach, and Varun Jampani. 2024. Sv3d: Novel multi-view synthesis and 3d generation from a single image using latent video diffusion. In *European Conference on Computer Vision*. Springer, 439–457.
- [28] Yiming Wang, Qin Han, Marc Habermann, Kostas Daniilidis, Christian Theobalt, and Lingjie Liu. 2023. Neus2: Fast learning of neural implicit surfaces for multi-view reconstruction. In *Proceedings of the IEEE/CVF International Conference on Computer Vision*. 3295–3306.
- [29] Xinyue Wei, Kai Zhang, Sai Bi, Hao Tan, Fujun Luan, Valentin Deschaintre, Kalyan Sunkavalli, Hao Su, and Zexiang Xu. 2024. MeshLRM: Large Reconstruction Model for High-Quality Meshes. *arXiv preprint arXiv:2404.12385* (2024).
- [30] Rundt Wu, Ben Mildenhall, Philipp Henzler, Keunhong Park, Ruiqi Gao, Daniel Watson, Pratul P Srinivasan, Dor Verbin, Jonathan T Barron, Ben Poole, et al. 2024. Reconfusion: 3d reconstruction with diffusion priors. In *Proceedings of the IEEE/CVF conference on computer vision and pattern recognition*. 21551–21561.
- [31] Chao Xu, Ang Li, Linghao Chen, Yulin Liu, Ruoxi Shi, Hao Su, and Minghua Liu. 2024. Sparp: Fast 3d object reconstruction and pose estimation from sparse views. In *European Conference on Computer Vision*. Springer, 143–163.
- [32] Jiale Xu, Weihao Cheng, Yiming Gao, Xintao Wang, Shenghua Gao, and Ying Shan. 2024. Instantmesh: Efficient 3d mesh generation from a single image with sparse-view large reconstruction models. *arXiv preprint arXiv:2404.07191* (2024).
- [33] Lior Yariv, Jiatao Gu, Yoni Kasten, and Yaron Lipman. 2021. Volume rendering of neural implicit surfaces. *Advances in Neural Information Processing Systems* 34 (2021), 4805–4815.
- [34] Jonathan Young. 2021. Xatlas.
- [35] Zhizhuo Zhou and Shubham Tulsiani. 2023. Sparsefusion: Distilling view-conditioned diffusion for 3d reconstruction. In *Proceedings of the IEEE/CVF Conference on Computer Vision and Pattern Recognition*. 12588–12597.